Article

by Nuria Sánchez-Pastor[1]*, Omid Fesharaki[2], and Isabel Hernando-Alonso[3]

A multi-technique approach to characterize the composition and color of the fossil remains of the "Húmera Paleontological Site" from Spain

[1] Departamento de Mineralogía y Petrología. Facultad de Ciencias Geológicas. Universidad Complutense de Madrid. Ciudad Universitaria, 28040, Madrid, Spain; *Corresponding author, *E-mail: nsanchez@ucm.es*
[2] Departamento de Didáctica de las Ciencias Experimentales, Sociales y Matemáticas. Facultad de Educación. Universidad Complutense de Madrid. Ciudad Universitaria, 28040, Madrid, Spain
[3] Centro Nacional de Investigación sobre la Evolución Humana. Paseo Sierra de Atapuerca, 3. 09002 Burgos, Spain

(Received: July 21, 2023; Revised accepted: May 5, 2024)

https://doi.org/10.18814/epiiugs/2024/024008

This paper combines a variety of physicochemical non-destructive techniques to obtain a knowledge of the chemical and mineralogical composition of the scarce fossil bones from the Húmera paleontological site (Madrid, Spain). The main classification of the samples has distinguished six colors: red, gray, blue, white, light yellow and green. μ-XRD and Raman spectroscopy have been correlated to study the structure and to distinguish between fluorapatite, chlorapatite, bioapatite and carbonated bones. The bones have further been classified in three main types. Type I includes gray, green, white, and blue samples, classified as fluorapatite and chlorapatite containing organic matter and adsorbed water. Type II, includes the red sample classified as bioapatite, showing broad Raman bands and μ-XRD peaks due to the lattice disorder created by the B-type substitutions emerging from a high matter content. Type III sample (yellow) shows a complete replacement of apatite by calcite which induce the high porosity of the sample. Diagenetic changes add further complexity to the structure of fossil bones, not only by new ionic substitutions but also in terms of biogenic or authigenic phases that form in the fossilizing bone. The multi-technique approach from a broad interdisciplinary perspective enables a better understanding of bone fossilization.

Introduction

The Húmera paleontological site occupies a surface extension of about 4000 m^2. This site was discovered in April 2008 and several excavation campaigns were carried out for the following three years (Fesharaki, 2016). Currently, despite the paleontological heritage law should have protected this site, it is covered by containment and beautification structures (Fesharaki et al., 2021). Due to its recent discovery and the very rapid covering of the site, only preliminary studies on the fauna association registered and the taphonomic and biostratigraphy characteristics have been done (Menéndez Gamella et al., 2010; Cárdaba et al., 2013). Since bone can record information concerning past habits (paleodiets, migration, climates), these materials have an important place in natural history. These changes can be observed in the form of changes in their texture, structure, as well as in their chemical and isotopic composition (Chadefaux et al., 2009). The knowledge of the extent and sequence of the diagenetic transformations is essential to infer paleoenvironmental and geological information.

Bones are composite materials constructed from an association of an organic phase constituted mainly by organized collagen fibres (collagen type I), a mineral phase which corresponds to a bioapatite, i.e. carbonated apatite nanocrystals, and water (Weiner and Price, 1986; Weiner et al., 1999). The fossilization process is a highly complex phenomenon which leads to the preservation of the skeletal material over geological time involving morphological, compositional, structural, and mechanical alterations (Clarke and Barker, 1993; Hedges, 2002; Reiche et al., 2002; Trueman et al., 2004). In the pre-diagenetic conditions (i.e., previous stage to the bone burial), microfossils undergo changes mainly due to intake of predators and to abrasion and degradation caused by environmental factors (Hedges and Millard, 1995; Trueman, 2004). However, during the diagenesis, with the introduction of the diagenetic solutions, chemical components diffuse into the bioapatite and become absorbed on the crystal surfaces or cause recrystallization of the apatite (Millard and Hedges, 1996; Kohn et al., 2008). The nano to microcrystalline structure of bioapatite has several sites for cations and anions. This means that is a complicated non stoichiometric form of hydroxyapatite $Ca_5(PO_4)_3(OH)$ which incorporates several elemental substitutions and can be approximated with the formula $(Ca,Mg,Na,Sr,Fe)_5(PO_4, CO_3)_3$ (CO_3, H_2O, OH, F, Cl) (Montel et al., 1981; Elliot, 2002). Bone diagenesis have also been associated with a variety of coupled substitutions maintaining neutrality by substitutions of ions with similar charges or vacancies elsewhere (Elliot et al., 1994; Trueman et al., 2004). The most abundant substitution is carbonate (Figueiredo et al., 2010) and depending on its crystal position can be classified as "A-Type", when carbonate is at the hydroxyl

position, or "B-Type" when substitutes the tetrahedral phosphates groups (McConnell and Gruner, 1940; Rey et al., 1990). Despite the low carbonate content that bioapatites can take (3-8 wt.%), it has been found that this substitution decreases bone crystallinity and accelerates its biodegradation rate (Figueiredo et al., 2010).

It is crucial to understand the origin of the different colours to provide a clue about depositional conditions and past environments. The paleontological materials shown in this research have been the focus of some studies in the past years (Menéndez Gamella et al., 2010; Cárdaba et al., 2013; Fesharaki, 2016) where the major goal has been to understand the taphonomic history of the fossil studying the sediments characteristics and the reconstruction of the paleontological interpretation. The origin of the different colors found in the samples remains elusive. Several and serious research efforts have tried to understand the origin of the color of paleontological samples. However, this topic is a subject of controversy (Weiner et al., 1998; Robles et al., 2002; Michel et al., 2006; Dauphin et al., 2023). The wide range of colours found in the fossil bones of micromammals in this site is a very remarkable feature (Hernando-Alonso et al., 2016, Fesharaki et al., 2021). This attribute is uncommon in the palaeontological record and there is debate about the causes of these chromatic variations. While some authors relate them to high temperatures in pre-diagenetic conditions (e.g., environmental fire; Rhodes et al., 2016), others mention bacterial action (Jans et al., 2004), ion exchange processes between palaeontological remains and diagenetic fluids (Nielsen-Marsh and Hedges, 2000) or changes in the pH of the sediment fluids that host the fossils (Nielsen-Marsh et al., 2007). The current research focusses on the mineralogical evolution of the rodent bones and the possible origin of the different colors shown in the samples as a proposed model based on limited number of specimens (in most of the cases only 1 or 2 samples were available for their study; up to 4 in the case of the white bones). Thus, a selection of non-destructive techniques has been applied to carry out the mineralogical study of the bones to infer the possible cause of the coloring. Thermogravimetry and differential scanning calorimetry (TGA-DSC) were used to estimate the organic matter content, but they cannot distinguish between different mineral compounds. Micro-XRD was useful to an initial approach of the F/Cl content and to distinguish between the apatite and carbonated samples. The same observation was enhanced using Raman spectroscopy and Energy-dispersive X-ray spectroscopy. Complementary chemical analyses were obtained by using an electron microprobe (EMPA). Finally, scanning electron microscopy (SEM) provided information about textural and mineralogical features of the surfaces.

Geological Setting and Materials

The Húmera Paleontological site is located in the western part of the Madrid Basin between two sandy alluvial fans (Torres et al., 1995), and belongs to the detritic facies of the mid-distal zones of Miocene Intermediate Unit of the Madrid Basin (Megias et al., 1983; Menéndez Gamella et al., 2010). These arcosic fans were formed by the erosion of plutonic and high-grade metamorphic rocks of the Central System (Fesharaki et al., 2015; Fesharaki, 2016). In the distal areas of the alluvial fans, clay and carbonate materials have been deposited revealing lacustrine and marshy areas where clay minerals and continental carbonates have been precipitated (Doval et al., 1985; Calvo et al., 1989). The stratigraphic records have been studied by Menéndez Gamella et al. (2010). From the base to the top of the succession: H1 and H2 are sandy units containing macromammal remains; H3 and H4 are silt clayey units separated by a calcrete level; and H5 unit is a unit with mixed characteristics between the H4 and the edaphic horizon (Fesharaki, 2016; Fesharaki et al., 2021). The total thickness of the succession is 3.60 meters. The first two sections (H1 and H2) have been assigned to debris flow type processes, with interruptions in the detrital sedimentation that have assisted the formation of incipient laminar carbonate palaeosoils (Menéndez Gamella et al., 2010). The three upper sections (H3, H4 and H5) have been assigned to palustrine-lacustrine environments with clay settling processes and periodic input of shaly sediments from the more distal parts of the alluvial fans (Menéndez Gamella et al., 2010). According to magnetostratigraphic studies of the Madrid Basin, the Intermediate Unit in the western part shows a sedimentation rate of about 4.0 to 4.7 cm/ka (Montes et al., 2006), therefore, the sedimentary succession of Húmera site would represent a time span of about 77-90 thousand years (Fesharaki, 2016). According to Fesharaki et al. (2021), the different levels described in the Húmera deposits show a similar mineralogy, in which tectosilicates (quartz and feldspars) and calcite prevail, together with clay minerals (mainly smectites, but also kaolinite and illite). However, these authors highlight the coexistence of different smectite phases (mainly montmorillonite and beidellite). This fact could indicate different transformation processes from pre-existing minerals (inherited from source areas) or intermediate transformation phases. These results are consistent with an environment with contrasted water seasonality and with the previously described sedimentary environments of alluvial fans carrying minerals inherited from the source area and palustrine-lacustrine zones. The bones for the present study were obtained from the level denominated in that work as H3 which enclosed abundant remains of microvertebrate fossils. The sedimentary environment is described as mid-distal alluvial fans with ephemeral ponds (Menendez Gamella et al., 2010, Fesharaki, 2016). The faunal association is made up of the taxa *Gomphotherium angustidens, Heteroprox moralesi*, *Anchitherium sp* and rodents of the order *Rodentia* and *Lagomorpha* (Cárdaba et al., 2013; Fesharaki, 2016). The taxonomically identifiable anatomical elements of the micromammal's fossils (almost exclusively molars) found until the burial of the site totaled 210 (Menéndez Gamella et al., 2010; Cárdaba et al., 2013). The taxonomic study and the biostratigraphic analysis using the association of fossils found at Húmera fossils site have allowed to place the site in biozone E (13,8 to 14,1 m.y.), belonging to middle Aragonian (Middle Miocene) (Menéndez Gamella et al., 2010; see discussion in Cárdaba et al., 2013). The first taphonomic observations have emphasized different states of conservation of the fossil remains, assigning them different taphonomic trajectories. This is a common feature in this kind of sedimentary environments (Domingo et al., 2017). However, some other characteristics of the microvertebrates fossils are less frequent, i.e., the total dissolution of the dentin in most of the molars, the greater presence of the third molars compared to the rest of the teeth, and the wide range of colors of the fossil skeletal remains (Menéndez Gamella et al., 2010). The last characteristic and the fact that the microvertebrates fossils are only concentrated in a section of a few centimeters (called H3, with a maximum thickness of 20 centimeters and a confirmed lateral extension of one meter) have

inspired the present study.

Methods

The management and research team of the Somosaguas and Húmera Paleontological site carried out the processing (washing-sifting) and the subsequent separation of the microvertebrate fossils under the magnifying glass of the materials removed from the H3 level of the Húmera site. The molars were used for taxonomic purposes and are currently in the National Museum of Natural Science (CSIC). The skeletal remains were given to the reservoir researchers for the taphonomic, geochemical and mineralogical studies. For the mineralogical study of the present work, the bones have been classified by using a magnifying glass according to their color in six classes: red bones (redB), gray bones (grayB), blue bones (blueB), white bones (whiB), green bones (greB) and light yellow bones (yellB) (Fig. 1).

After being classified, white bones (whiB) were used to estimate the possible organic material content by means of the TGA-DSC analysis. Subsequently, a representative bone of each color was selected, embedded in Epoxy resin, and polished to reach the center of the bones and avoid superficial contamination. The result of this treatment was a smooth and homogenous surface ideal to carry out the study by Raman spectroscopy, energy-dispersive X-ray spectroscopy (EDXS), electron microprobe (EMPA) and X-ray microdiffraction (μ-XRD). Yellow samples (yellB) were also imaged by scanning electron microscopy in order to see the porosity of the samples.

Raman Spectroscopy

The Raman spectra were collected at room temperature with a confocal Thermo Fisher DRX Raman spectrometer equipped with a confocal microscope with a point-and-shoot Raman capability of 1 μm spatial resolution. This microscope belongs to the National Museum of Natural Sciences from Madrid (Spain). The objective selected was of 10x magnification, with a numerical aperture of 0.9, together with a laser source at 785 nm at 8-10 mW in a laser mode power at 100%. The laser was always focused at a minimum depth of 5 μm below the surface of the sample. The average spectral resolution of the Raman shift ranging from 70 to 3,400 cm^{-1} was 2–4 cm^{-1}, i.e., grating 900 lines/mm, and a spot size of 2 lm. The system was operated under OMNIC 1.0 software selecting working conditions such as pinhole aperture of 25 μm and bleaching time of 1–2 s; four to seven exposures in 10 - 30 s depending on the sample (higher number and exposure times for the yellow samples (YellB). Peak deconvolution was carried out using the software package Fityk (Wojdyr, 2010).

X-ray Microdiffraction Analysis (μ-XRD)

The measurements were performed on the polished samples using a Panalytical X'Pert PRO diffractometer with CuKα radiation. The X-ray generator worked at a power of 45 kV and 40 mA, and the resolution of the instrument was determined using SiO_2 standards. The patterns were collected with 0.03º of step size in the angular range 20º–90º in 2θ, with counting time of 80 s per point. XRD-patterns were analyzed to evaluate quantitatively the mineralogical phases. Highscore Plus Software and Powder Diffraction File (PDF) were used to interpretate the XRD patterns.

Thermo Gravimetric Analysis (TGA) and Differential Scanning Calorimetry (DSC)

In comparison to the other techniques employed in this study, TGA is a destructive yet crucial method for estimating the mineral and/or organic content of the samples. In most cases, we had only one or two samples of each color. However, in the case of the white bones, we had more than three specimens. That is why these samples have been selected for the TGA study, since they have been the only ones capable of providing the necessary quantity (11mg) to estimate the organic material using a SDT – Q600 and Q – 200 simultaneously. Samples were heated from 20 ℃ to 1000 ℃ at a constant heating rate of 10 ℃/min, with continuous nitrogen flow.

Microprobe Analysis (EMPA) and EDXS Mapping

Carbon-coated polished samples were used for the microprobe measurements. The samples were analyzed for major and minor elements using a Jeol JXA 8900 microprobe at the National Center for Electron Microscopy (CNME) at the Complutense University of Madrid (Spain). The spot analysis were done with an acceleration voltage of 15 kV, a probe current of 10 nA and a defocused beam with a diameter of 5 μm. Distribution maps for major elements were measured with a dwell time of 5 ms at a beam time current of 20 nA at 10 kV.

Scanning Electron Microscopy (SEM)

Supplementary information about textural and mineralogical features of the carbon coated bone fragment samples were obtained by a JEOL JSM 6400, 40 kV. The only samples used for the textural and porosity study using SEM were the yellow samples. This was due to the fact that they were the only samples exhibiting surface porosity where other intergrown minerals could be distinguished. In the other samples, the surfaces appear dense with low porosity, and small fractures mostly covered by clay minerals.

Results and Discussion

The samples studied displaying the superficial characteristics and the different colors are shown in Fig. 1. There are six different classes with six diverse colors, red bone or redB (Fig. 1a and b), gray bone or grayB (Fig. 1c), blue bone or blueB (Fig. 1d), white bone or whiB (Fig. 1e), yellow bone or yellB (Fig. 1f), and green bone or greB (Fig. 1g). The fossil remains have similar sizes, ranging between 2.5 and 5.5 mm long. Bones do not show signs of abrasion or dissolution by intake which is a common feature in many deposits of microvertebrates. However, they show different conservation states. Some of them are complete and perfectly preserved (Fig. 1 d, e, f and g) but some other are fractured in their ends (Fig. 1 a and c).

In addition to the color and the conservation state, another feature categorized with these pictures is the porosity of the bones. As can be seen in Fig. 1, the surface of most of them is dense and perfectly pre-

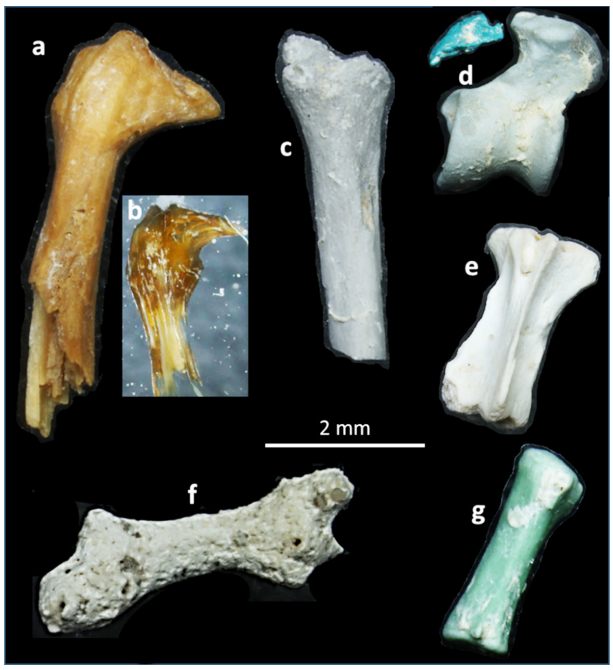

Figure 1. Pictures of the selected samples under magnifying glass showing the superficial characteristics and different colors. (a) Red bone (rebB), (b) bone from image (a) embedded in resin and showing the core of the sample and the homogeneous color, (c) gray bone (grayB), (d) blue bones (blueB), (e) white bone (whiB), (f) light-yellow bone (yellB), and (g) green bone (greB).

serve the compact bone. However, there are some fragments, like the ones shown in Fig. 1f, with a light-yellow color, showing a porous and irregular surface. Fig. 1b shows the same bone as in Fig. 1a but embedded in resin and polished to reach the core of the sample. This image confirm that red color is not only a superficial characteristic, but it is preserved over the sample.

Raman Study of the Structure of the Fossil Remains

The Raman spectra of the samples allow the analysis of the structure of the bones by means of the bonding configuration. Moreover, both, mineral and organic constituents of bones can be detected. The spectra shown in Fig. 2 are presented with a normalized intensity for easier comparison. The fluorescence, frequently induced in Raman examinations, was attenuated by increasing the exposure time of the laser. However, in some samples, the Raman study was problematic, and the background luminescence had to be subtracted from baseline computation. Several analyses were made on each sample to have representative results. Nevertheless, since the spectra did not vary more than 1 or 2 wave numbers in the different areas of the sample, the Raman shift was not significant and only one spectrum for sample is presented for better clarity.

From left to right, the bands shown in Fig. 2 correspond to the lattice modes Ca-CO_3, Ca-PO_4 and Ca_3-F found at low frequencies (100-350 cm^{-1}), the symmetric stretching ν_1 modes of the PO_4^{3-} and CO_3^{2-} units appear around 960-1085 cm^{-1}, amides bands and broad bands due to

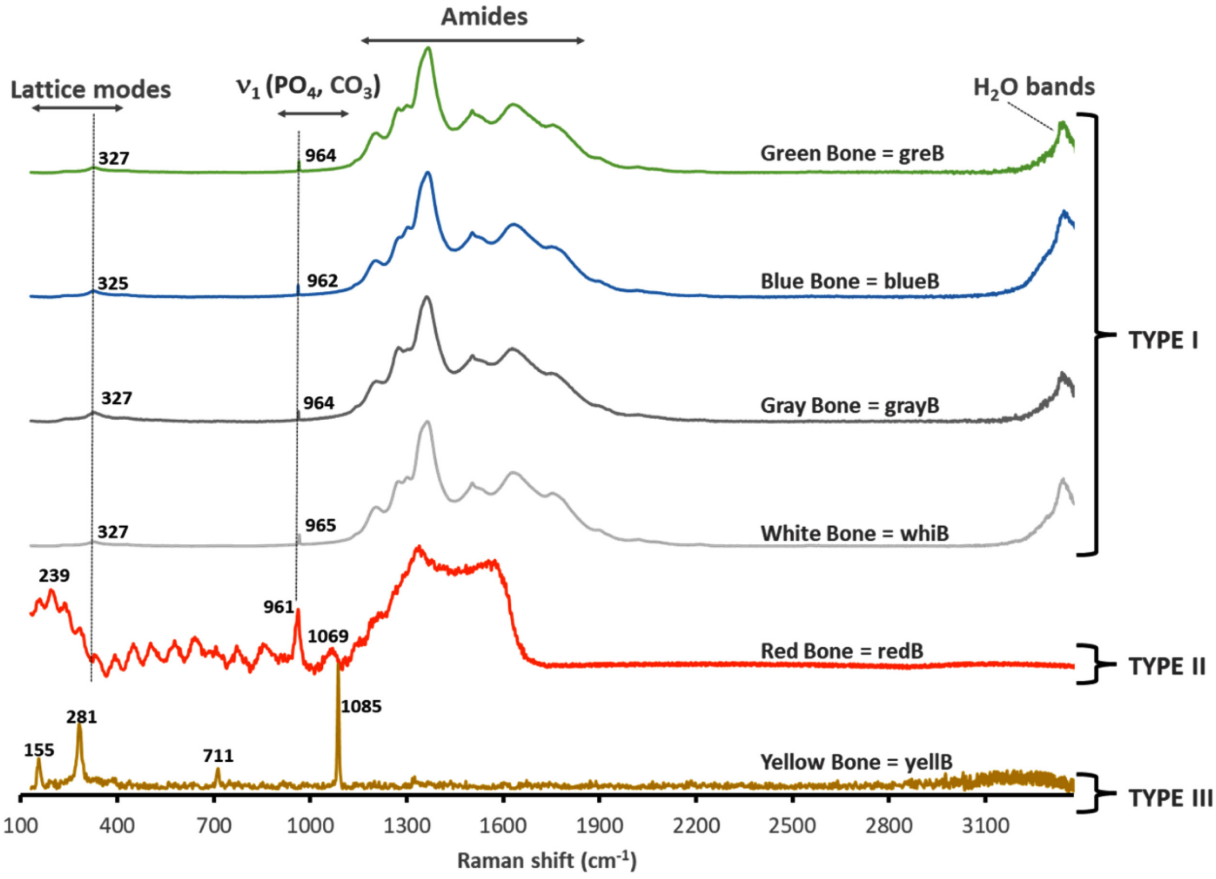

Figure 2. Raman spectra of the fossil remains showing the main bands. The abbreviation for each sample is shown next to the spectra. From bottom to the top: yellow (yellB), red (redB), white (whiB), gray (grayB), blue (blueB) and green bones (greB).

fluorescence could appear between 1200 and 1800 cm^{-1} and water bands can be seen at high frequencies (3,345 cm^{-1}). Judging by the differences observed at first glance, the samples can be classified into three types. (see Table 1 for band assignations: Penel et al., 1998; Carden and Morris, 2000; Tarnowski et al., 2002; Pennel et al., 2005; Antonakos et al., 2007; Thomas et al., 2007 Lebon et al., 2008, 2010).

Type I would include the grayB, greB, blueB and whiB samples where the typical ν_1 internal mode of the phosphate ion dominate the mineral part. These vibrations corresponding to the PO_4^{3-} units appear weaker and poorly defined as expected due to the high fluorescence of the samples. However, the intensities remain similar in all samples and the results can be correlated in the normalized spectra. The lattice modes bands at ~243 cm^{-1} and ~326 cm^{-1}, are assigned to the Ca-PO_4 and Ca_3-F vibrations, respectively. In addition, a multitude of bands with high intensity in the range from 1200-1800 cm^{-1} can be seen. These bands appear when the spectrum is overwhelmed by fluorescence and matches perfectly the spectra shown in the Rruff Project (Laetsch and Downs, 2006) for fluorapatite showing a broad scan with spectral artifacts. However, some bands obtained after the treatment of these data differ from the ones shown for the fluorapatite sample and have been related to the presence of organic matter (collagen bands: Amide I and III) (Tadic and Epple, 2004; Stathopoulou et al., 2008). The band at higher frequencies, 3,345 cm^{-1} corresponds to absorbed water on the surface of the samples (Carden and Morris., 2000; Wopenka and Pasteris., 2005; Antonakos et al., 2007). The presence of OH is usually confirmed by a group of vibrations modes in the region at ~3,500-3,600 cm^{-1} (Pieczka et al., 2020; Pasteris et al., 2004). Since no bands are seen on the area of the OH^- vibrations modes, it seems clear that these apatitic bones are not hydroxylapatite (HAp). This is consistent with the OH-absence in nanocrystalline bioapatites (Pasteris et al., 2004; Wopenka and Pasteris., 2005). The OH^- groups occupies the so-called channel site but this position can also be occupied by substituting ions like F^- (Fluorapatite, FAp) and Cl^- (Chlorapatite, ClAp). Among these anions, the one that best fits into the channel site due to its small ionic radius is F^-. Thus, Raman study would classify the components of Type I group as fluorapatite with most likely a minimum amount of organic matter and absorbed water. However, in the case of the blue sample (bluB), a slight Raman shift can be observed in the bands assigned to the Ca_3-F and to the symmetric stretching ν_1 mode of the PO_4^{3-} (see data in Table 1). This could imply a difference between the green, gray, and white samples, classified as fluorapatite, and the blue sample. This difference will be obvious after the XRD and microprobe analyses results shown in the next sections which label the blue sample as chlorapatite.

The redB sample show a different spectrum and would belong to the second type of samples (Type II). This sample was the most problematic for the Raman analysis due to the high fluorescence. As can be seen in Fig. 2, redB shows intermediate characteristics between samples from Type I and III. Moreover, this spectrum shows broader bands than the other five indicating a poor degree of crystallization distinctive of bioapatites (Mann, 2001; Pasteris et al., 2001). Following the study from Wopenka and Pasteris (2005), the broad bands can be attributed to the replacement of phosphate by carbonate which strains the crystal lattice and limits the size of the crystallite growing. The bands at 239, 280 and 328 cm^{-1} correspond to the Ca-PO_4, Ca-CO_3 and Ca_3-F vibrations modes, respectively. As in the case of the spectra belonging to Type I, the internal mode of the phosphate units, ν_1, has been assigned. However, there is an important shift with respect to the other samples, showing symmetric stretching of the phosphate group at 961 cm^{-1}. The downshift by 2-3 cm^{-1} has been reported for biological and synthetic carbonated apatite with high carbonate substitutions (Penel et al., 1998; Pasteris et al., 2004). The higher amount of carbonate in this sample shown by the presence of the Ca-CO_3 lattice modes, the broad bands, and the displacement of the PO_4 symmetric stretching is also supported by the presence of the bands at 707, 870 and 1,069 cm^{-1}. The first two assigned to the n_4 CO_3 mode and, the last one to the ν_1 CO_3. Moreover, there is a widespread assignment of the 870 and 1069 cm^{-1} CO_3 modes to B-type substitutions as a consequence of the maturing process suffered during the bone diagenesis (Rey et al., 1989; Sponheimer and Lee-Thorp, 1999; Stathopoulou et al., 2008; Fleet, 2009). In the region from 1,200-1,700 cm^{-1}, the bands are broad and difficult to assign but there are some peaks which could correlate with the Amides I and III and also with the artifacts from the fluorescence as in the case of Type I samples. Water and OH bands are not observed in this spectrum.

Finally, the yellB sample would belong one last type of samples (Type III) where clearly distinguishable peaks corresponding to calcite are observed (Fig. 2 and Table 1). The bands obtained at low frequencies, 155 and 280 cm^{-1}, were assigned to the Ca-CO_3 lattice modes and the bands at 711 and 1085 cm^{-1} correspond to the ν_4 and ν_1 modes of CO_3^{2-}, respectively. Only weak features, not detected after processing the data, indicative of residual phosphate and humidity are observed and no organic matter.

Qualitative Evaluation of the Phases by Micro-XRD

Figure 3 shows the μ-XRD patterns of the bones. From bottom to

Table 1. Raman bands (cm^{-1}) observed in the spectra of the samples and assignments

greB	blueB	grayB	whiB	redB	yellB	Band assignation
				280	155, 281	Ca-CO_3 Lattice Modes
243	243	244	243	239		Ca-PO_4 Lattice Modes
327	325	327	327	328		Ca_3-F Lattice Modes
				707 870*	711	ν_4 CO_3 *B-type CO_3^{2-}
964	962	964	965	961		ν_1 PO_4
				1069*	1085	ν_1 CO_3^{2-} / *B-type CO_3^{2-}
	1200-1900			1200-1700		Broad bands artifacts and Amides I and III
	3345					Absorbed water

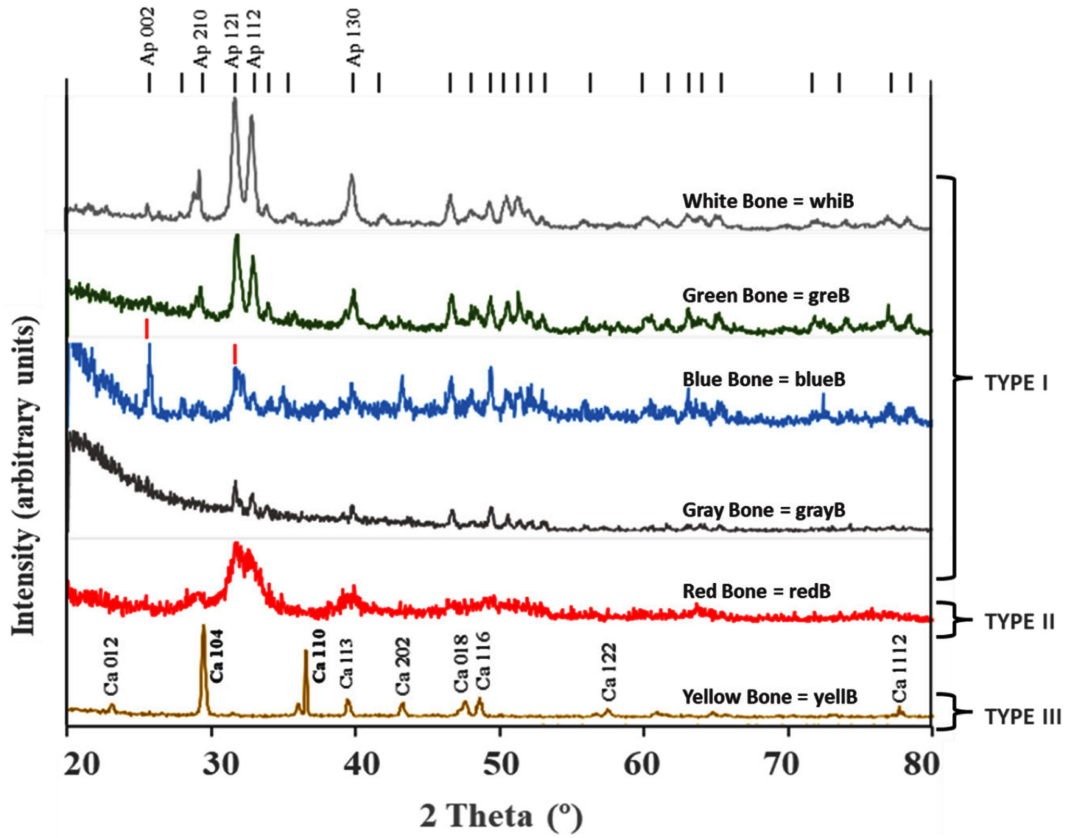

Figure 3. XRD diagrams. Corresponding positions of the diffraction peaks for calcite are indicated on the yellow pattern. The rest of the samples identified as apatite correlate with the black vertical bars showing the main position of the peaks for this phase. The two vertical red lines next to the blue diagram, indicate the reverse intensity of the 121 and 112 peaks and the high intensity of the 002 reflection for chlorapatite.

upper side of the diagram: yellB, redB, greyB, blueB, greB, and whiB bones. The patterns shown in this figure are not scale on the y-axes but are shown offset for clarity. The results obtained revealed the principal differences in the structure of the bones depending on the color and correlate with the Raman spectroscopy results. The main reflections for calcite are indicated next to the yellow profile (yellB) and the peaks of apatites are shown in the upper side of the diagram.

As can be seen, yellB is composed principally of calcite (Type III), redB (Type II) display extremely broadened diffraction peaks due to its nanocrystalline nature, but still the main reflections for apatite (121, 112 and 210) can be detected. Moreover, in comparison with Raman results, some differences can be observed among the patterns of the bones belonging to Type I. GrayB, blueB and greB bones reveal a clear sharpening of the 121 and 112 reflections belonging to apatite. However, the intensity of these reflections appears reversed in the blueB. This reverse intensity in the main peaks of the apatite phase together with the high intensity of the 002 reflection in the diagram of the blueB, correlates with the assignation of the bands to chlorapatite. This classification of the blueB is consistent with the slight Raman shift found in the Ca_3-F and the symmetric stretching ν_1 PO_4^{3-} modes found in this sample. Fluorapatite have been identify for grayB and greB. Finally, the diffraction pattern obtained for white samples (whiB) sharpens considerably showing a better identification of the peaks corresponding to fluorapatite. The sharpening of the peaks could indicate a higher grade diagenesis with an increase in crystallinity due to the decrease of the carbonate content and, probably, of the organic matter (Person et al., 1995; Lamsihar et al., 2015). The fact that the diffraction peaks are broader for the red pattern (redB) agrees with the crystal lattice change induced by the replacement of phosphate ions by carbonate seen in the Raman study. The crystallinity of the carbonated apatites (i.e., bioapatites, BioAp) decreases due to the lattice defects caused by the B-type substitution (McElderry et al., 2013; Xue et al., 2015).

Thermal Analysis to Estimate Carbonate and Organic Matter Content

The thermogravimetric analysis of the white sample (whiB, the only candidate for a destructive analysis) is depicted in Fig. 4. As can be seen, three inflection points can be identified. The first one between 20 – 200 ℃ corresponds to a weight loss of 2.37% and is correlated with the evaporation of water. The second inflection point detected between 200 and 550 ℃. The weight loss of 3.72% is attributed to the decomposition of organic matter (which confirm that the part of the Raman bands in the range from 1,100–1,800 cm^{-1} belong to the Amides). A third stage between 600 and 950 ℃, with a weight loss of 3.82%, is associated to the decomposition of carbonate. From these data, one could expect total percentages of ~90% in the EMPA analysis.

Chemical Composition of the Fossil Remains (EMPA and EDXS)

One concern when analysing these materials is their variable poros-

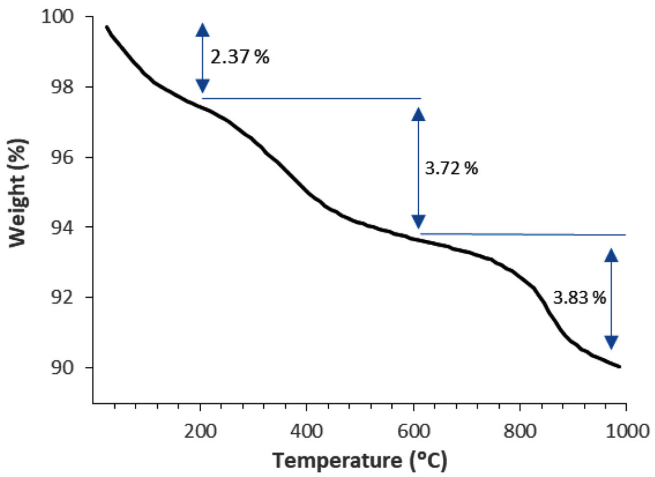

Figure 4. TGA thermogram of a white sample showing three inflection points.

ity which can affect the final composition. Another difficulty was the alteration of the bones and the secondary mineral phases formed in the porosity during the diagenesis (principally, silicate minerals). In order to minimize these variations, element maps of the polished surfaces of the bones were taken. By using these maps, it was possible to clearly distinguish the porosity and the secondary mineral phases and hence, to choose the best area for the analyses. Figure 5 shows an example of this study carried out on the blue bone (blueB) to choose the best area. As a first approximation, some analyses were taken all over the sample (point analysis in Fig. 5a). However, due to the variables mentioned above (secondary mineral phases and empty pore spaces), very fluctuating results were obtained. To solve the problem, element maps for Ca, P, F, Cl, Si, Fe, Cu, Mg, K, Na, Fe, Sr, Ba, Cu, Mn and Al were taken on detailed areas of the surface. After considering the composition maps, the best area for the analyses was chosen (profile I-II in Fig. 5b). As can be seen in Fig. 5g, the secondary mineral phases, probably silicates, are evident by an increase in the aluminium content. Another interesting feature that can be noticed by examining the element maps of the blue bone is the higher Cl^- concentration (Fig. 5e) with respect to F^- (Fig. 5f) which correlates with the chlorapatite structure given by Raman and XRD analysis.

Figure 6a shows the polished surface of a yellow sample (yellB). The high porosity of these samples and the area chosen for the composition analyses (red profile in Fig. 6a) can be observed. Figure 6b displays a SEM image showing the high porosity of these samples. Calcite rhombohedra replacing the original bone and some sheet-like minerals (i.e., smectites) were identified. As can be seen in the element maps for Si and Al (Fig. 6 c and d), almost the complete surface of the sample is composed of secondary silicate phases indicating an important alteration. The dark area of the bone was the one chosen for the analysis and, as expected from the Raman and XRD results, very low phosphate concentrations were obtained. The high porosity is attributed to the important decrease in the molar volume produced by the replacement of the original apatite bone by calcite.

This pattern of high porosity related to an increase of the secondary mineral phases is not shown in the red and green bones where no secondary phases were observed and only Ca was clearly distinguishable in the element maps. Moreover, in the green bone, the porosity was easy to avoid and probably belongs to the original porosity of the bone with a high and homogenous size of the pore spaces (Fig. 7a). The red bone showed no porosity and homogeneous element maps (Fig. 7b).

The chemical composition of the samples is summarized in Table 2. Bold values shown in the table have been used to emphasize the important data for the discussion of the chemical composition. In the table, the number of analyses used to determine the average of each compound can be seen in the second raw. The average concentration of the main oxides (P_2O_5, SiO_2, FeO, CaO, MgO, MnO, SrO, Na_2O, SO_3, K_2O and Al_2O_3) and some important elements (F and Cl) are shown first together with the standard deviation next to each value. The total sum in percentage can be observed in bold values in the middle raw of the table. After the total oxide sum, some ratios have been calculated for the interpretations.

The P_2O_5 concentration has been used as the denominator of the

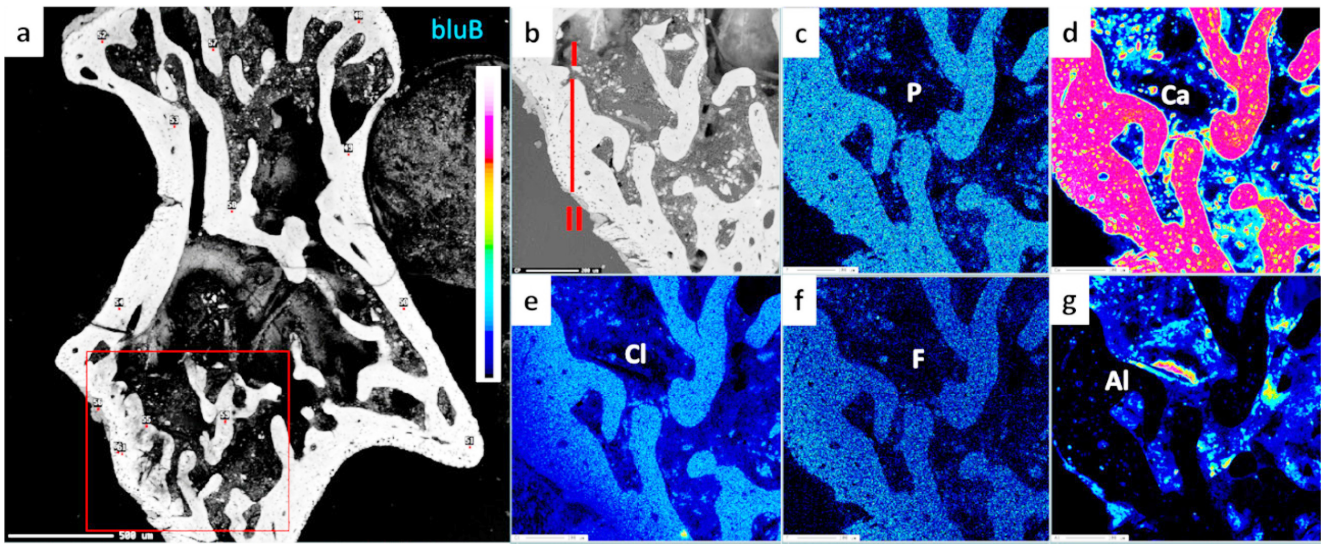

Figure 5. Microprobe study of the blue bone. a) Backscattered image showing the chosen area in red. b) Analyses profile. c, d, e, f and g) Element maps for P, Ca, Cl, F and Al.

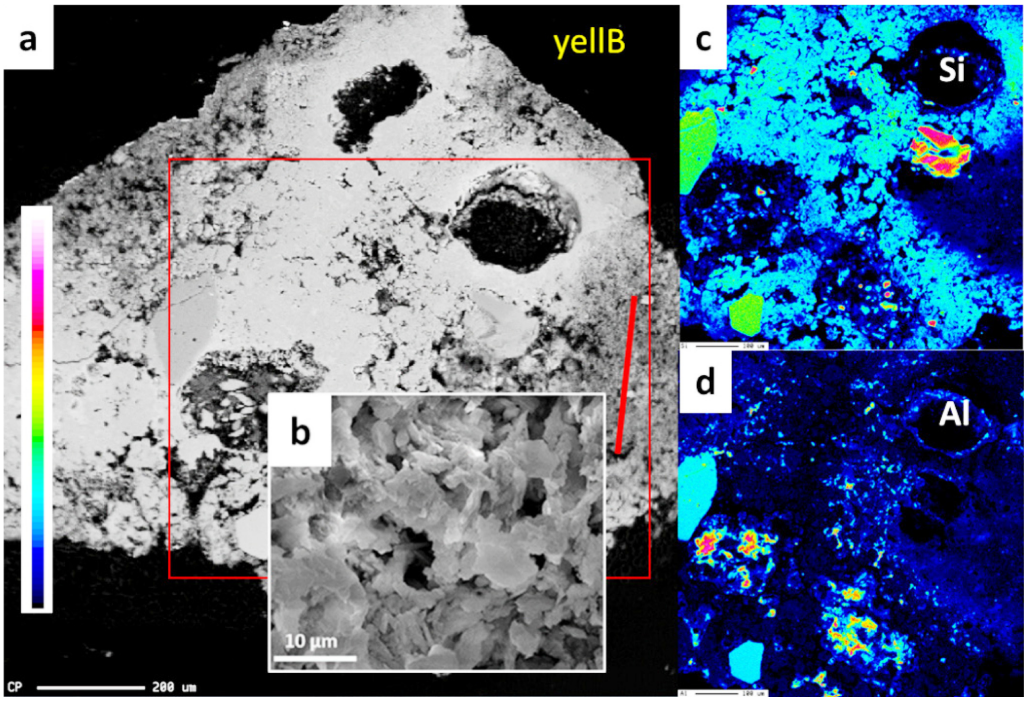

Figure 6. EMPA and SEM study of the yellow bone. a) Backscattered image showing the mapped area and the analysis profile in red. b) SEM image showing the intense porosity and the carbonate replacement. c) Element map for Si. d) Element map for Al.

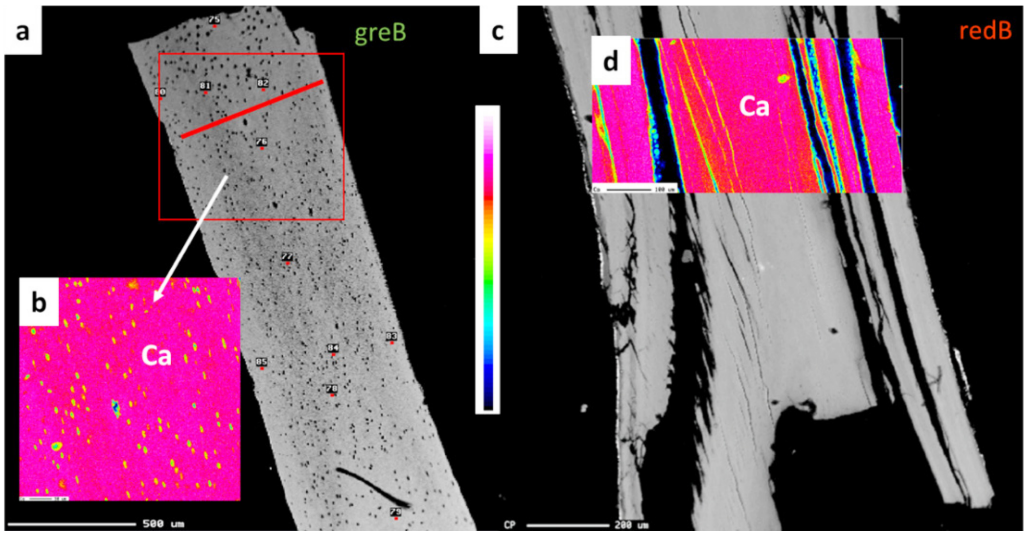

Figure 7. EMPA study of green and red bones. a) Green bone showing the mapped area and the analyses profile. b) Element map for Ca. c) Absence of porosity in the red bone d) Element map for Ca.

ratios shown in the table to provide equivalent interpretations and conclusions regarding chemical variations induced by the diagenetic processes. As can be seen, the concentration of the main oxides, CaO and P_2O_5 vary about 0.2 to 1.7% (standard deviation in Table 2). The rest of the oxides and elements analysed show minor concentration variations. Bold numbers show the greater variations that will be discussed in the next section. It is important to note that the total oxide sum is always less than 100 wt.% leading once more to differentiate the three types of samples mentioned before: Type I ranging from 90.1 to 96.21 wt.% (consistent with the thermal analyses), Type II with a total oxide sum of 80.1 wt.% due to the presence of B-type carbonate, the empty pore spaces and, probably, a higher content of residual organic substances as discussed from Raman and XRD analyses in the red bone. And type III with a considerably low sum of 39.36 wt.% due to the replacement of the yellow bone by calcite. Since it is clear that the yellow bone is completely replaced by carbonate at this point, this sample is not considered for the discussion from here on.

The CaO concentration also indicates systematic differences between the three types of samples. However, the differences in the rest of the elements content reflect dissimilarities between the samples belonging to Type I (gray, white, green, and blue bones). In order to facilitate compositional comparison between the different samples, some

Table 2. Average chemical compositions of fossil bones. Bold numbers show large variations with respect to the other values

Sample	TYPE I								TYPE II		TYPE III	
	greB		blueB		grayB		whiB		redB		yellB	
Analyses	30		26		18		25		20		15	
	Ave	1σ	Ave	1σ	Ave	1σ	Ave	1σ	Ave	1σ	Ave	1σ
P_2O_5	39.50	0.50	37.24	0.83	37.29	1.31	37.07	0.28	31.70	1.20	**0.16**	0.03
SiO_2	0.120	0.150	*b.d.l.*	*b.d.l.*	*b.d.l.*	*b.d.l.*	**0.920**	0.250	*b.d.l.*	*b.d.l.*	2.840	0.820
FeO	0.110	0.053	0.018	0.016	0.051	0.021	**0.380**	0.070	0.013	0.020	0.270	0.090
CaO	54.56	0.67	50.41	1.01	53.20	0.70	51.01	0.60	**46.70**	1.70	**28.60**	3.26
MgO	*b.d.l.*	*b.d.l.*	*b.d.l.*	*b.d.l.*	*b.d.l.*	*b.d.l.*	0.103	0.027	**0.350**	0.040	0.600	0.100
MnO	0.012	0.022	0.018	0.021	0.011	0.015	0.019	0.020	0.012	0.017	0.016	0.020
SrO	0.110	0.040	0.099	0.027	0.110	0.030	0.062	0.019	0.118	0.020	0.017	0.031
Na_2O	0.102	0.030	0.110	0.030	0.110	0.020	0.380	0.045	0.510	0.040	0.120	0.038
F	1.690	0.068	0.930	0.160	2.140	0.100	2.000	0.060	0.940	0.230	0.019	0.023
Cl	0.097	0.018	**1.780**	0.280	0.082	0.026	0.140	0.016	0.150	0.050	0.430	0.081
SO_3	0.006	0.009	0.004	0.008	b.d.l.	b.d.l.	b.d.l.	b.d.l.	b.d.l.	b.d.l.	0.010	0.010
K_2O	0.007	0.006	0.004	0.004	0.006	0.007	0.022	0.013	0.006	0.007	0.142	0.073
Al_2O_3	0.250	0.007	0.250	0.180	0.250	0.120	0.430	0.046	0.028	0.021	1.260	0.440
TOTAL	**96.21**	1.02	**90.10**	1.60	**93.20**	1.31	**92.54**	0.73	**80.10**	2.90	**39.36**	3.80
Ca/P	**1.75**	0.02	**1.71**	0.02	**1.81**	0.01	**1.74**	0.01	**1.86**	0.03		
CaO/P_2O_5	1.38	0.02	1.35	0.02	1.43	0.01	1.38	0.01	1.47	0.03		
MgO/P_2O_5	*b.d.l.*	*b.d.l.*	*b.d.l.*	*b.d.l.*	*b.d.l.*	*b.d.l.*	0.0028	0.0007	0.0110	0.0013		
FeO/P_2O_5	0.0029	0.0015	0.0005	0.0004	0.0014	0.0006	**0.0104**	0.0019	0.0040	0.0040		
Na_2O/P_2O_5	0.0026	0.0008	0.0031	0.0008	0.0028	0.0005	**0.1030**	0.0013	0.0160	0.0010		
F/P_2O_5	0.0430	0.0170	0.0250	0.0045	0.0560	0.0023	0.0540	0.0019	0.0300	0.0070		
Cl/P_2O_5	0.0025	0.0005	**0.0470**	0.0070	0.0022	0.0007	0.0038	0.0004	0.0050	0.0010		
MgO/Na_2O	*b.d.l.*	*b.d.l.*	*b.d.l.*	*b.d.l.*	*b.d.l.*	*b.d.l.*	0.28	0.09	0.78	0.12		
SrO/P_2O_5	0.0028	0.0015	0.0027	0.0007	0.0029	0.0008	0.0017	0.0005	0.0037	0.0008		
F/(F+Cl)	**0.954**	0.009	**0.350**	0.070	**0.960**	0.013	**0.931**	0.006	**0.850**	0.073		

data shown in Table 2 have been plotted in Fig. 8. The first notable observation in the total oxide sum (Fig. 8a), which is always less than 100 wt. %, and the CaO/P_2O_5 ratios (Fig. 8b) is the clear difference of the red bone (redB) sample with respect to the others. As can been seen in both plots shown in Fig. 8 a and b, the values of the red sample in both cases stands out over the other samples with a minimum (total oxide sum) or a maximum value (CaO/P_2O_5). Another remarkable observation in these two plots from Fig. 8a and 8b is the light deviation of the blue sample (blueB) inside the trend of Type I samples in both cases. This deviation becomes unmistakable when considering the plot depicted in Fig. 8c showing the F/(F+Cl) ratio. In this case, the deviation showing a lower F concentration with respect to Cl, correlates with the XRD results where the blue bone pattern was assigned to a chlorapatite instead of fluorapatite. There are also differences in the FeO/P_2O_5 content with a light increase in the green (greB) and red (redB) samples and a clear enrichment in the white sample (whiB) (Fig. 8d). Another interesting point of the composition table is the high Na and Mg concentration shown in the white (whiB) and red (redB) samples which is clearly perceived in the MgO/P_2O_5 and NaO/P_2O_5 ratios plotted in Fig. 8e and 8f, respectively. The concentration of the remaining analysed components is consistently very low, often close to or below the detection limits. These composition data shown in Table 2 and the ratios plotted in Fig. 8 are discussed in the next section to determine the possible causes of color of the different samples.

Ionic Substitutions and Possible Causes of Color

The above information demonstrates that the bones belonging to the Types I, II and III can be clearly differentiated by either XRD or Raman spectroscopy. However, the exact correlation between chemical composition and the observed color of the samples is considerably more complicated. Color has been sometimes related to the presence of a specific chemical element (Shipman et al., 1984; Shahack-Gross et al., 1997; Robles et al., 2002; Borrero, 2003) or to confirm that bones were burnt (Michel et al., 1998; Michel et al., 2006).

The structure and chemistry of apatite allow for numerous substitutions, including a multitude of metal cations (i.e., K, Na, Mn, Ni, Cu, Co, Zn, Sr, Ba, Pb, Cd, Sb, Y, U) and REEs that substitute for Ca in the structure, and anionic complexes (i.e., AsO_4^{3-}, SO_4^{2-}, CO_3^{2-}, SiO_4^{4-}, etc.) that replace PO_2^{5-} (Pan and Fleet, 2002). Indeed, apatite incorporates half the periodic table in its atomic arrangement. These substitutions are usually in trace concentrations, but large concentrations and even complete solid solutions exist for certain substituents. This complex and variable chemistry has great implications. The presence of carbonate

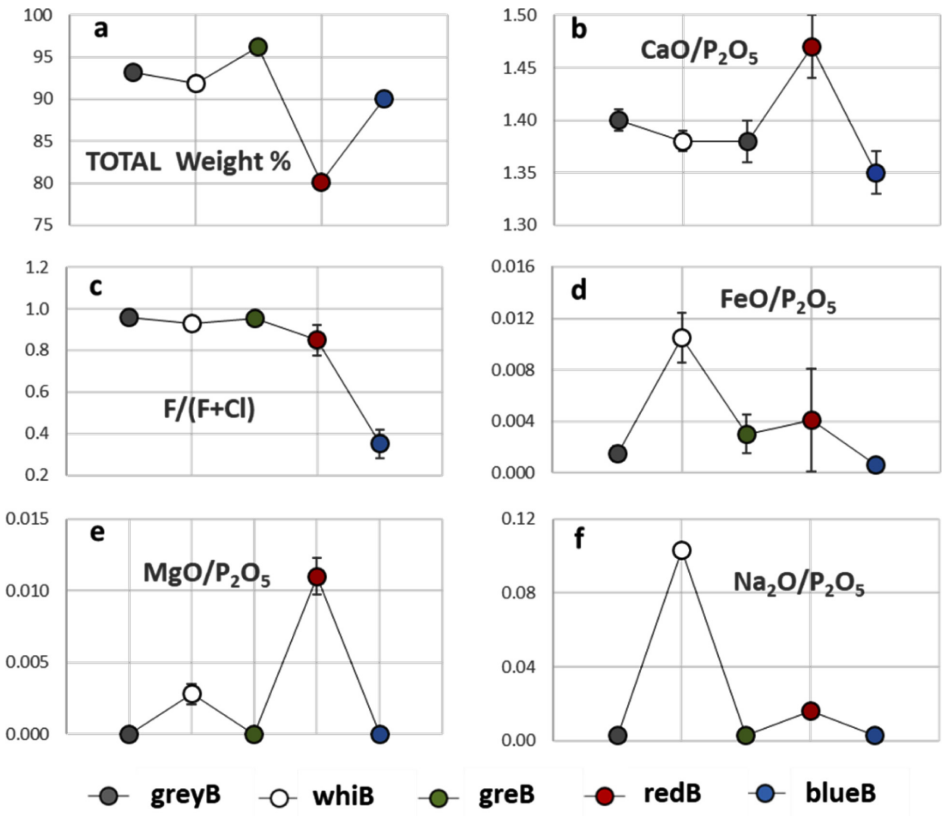

Figure 8. Comparison of the average chemical compositions of all fossil materials.

is of particular importance in bioapatites. Much controversy still exists about the carbonate incorporation into the apatite lattice. Several authors have recognised the presence of substantial amounts of carbonate in biological apatites (McConnell and Gruner., 1940; LeGeros et al., 1969; Rey et al., 1989; Gadelata et al., 1996; Daculsi et al., 1997; Camacho et al., 1999; Timlin et al., 1999; Elliot, 2002; Gross and Berndt, 2002). As commented before, two different apatites can be originated as a consequence of the carbonate substitutions, one in which the carbonate planar ion replaces the tetrahedral phosphate group called B-type substitution and, another in which the carbonate ion replaces the OH^- group in the channel site called A-type substitutions.

From the results shown above (see Table 3 for a summary of the results obtained with the different techniques), it seems clear that all the bones contain carbonate at some extent, being the red bone (redB) the one with a higher amount (bands assigned to B-type carbonate). Since synthetically A-type apatite can only be produced at very high temperatures and B-type apatite does not need elevated temperatures to form, the structure of the red bone is associated with the second type substitutions. Moreover, predominantly, the carbonate ions are present as B-type carbonates in natural bone minerals (Rey et al., 1989; Landis et al., 2003; Fleet, 2009). This together with the higher organic matter content emerging from the broad Bragg peaks due to the small crystallite size and high lattice disorder (Piga et al., 2011) leads to classify this bone as bioapatite. Accordingly, the red color (which could also be defined as a brownish dye) of this sample is attributed to the high content in organic material with respect to the other samples due to the less degree of maturity seen in the micro-XRD pattern. The very low concentrations of K_2O, SiO_2 and Al_2O_3 (see, Table 2) indicate that

Table 3. Summary and classification of the main results obtained by Raman spectroscopy, XRD, and Microprobe analysis

Sample Type	Sample color	Raman	DRX	Ca/P	F/(F+Cl)	Total weight %
Type I	greB	FAp	FAp	1.75	0.95	96
	grayB	FAp	FAp	1.81	0.96	93
	whiB	FAp	FAp	1.74	0.93	92
	blueB	FAp	ClAp	1.71	0.35	90
Type II	redB	Bio-Ap	Ap (B-type CO_3^{2-})	1.86	0.85	80
Type III	yellB	Calcite	Calcite			39

crystallization or mechanical introduction of silicate phases into the fossil during diagenesis is not of importance. The higher MgO content (Fig. 8e) is also related to the less maturation grade of this sample. High concentrations of this element in fossils have been related to stages at the beginning of the maturation process (Kalvoda et al., 2009; Sabel et al., 2009; Brügmann et al., 2012). According to Nicholson (1993), brown bones do not contain Fe oxides. They are tarnished by humic components when they are within or in direct contact with soils which correlates with the maturation state of our red bone.

The samples belonging to Type I were divided into fluorapatite (whitB, grayB and greB samples) and chlorapatite (blueB) by analysing the XRD patterns. The incorporation of F^- instead of OH^- produces a better fit of the anion in the channel position and it can occur so rapidly and even at room temperature (Freeman et al., 2001; Hughes and Rakovan, 2002). Typically, fluorapatite is the preserved mineral in fossil bones: during the burial of bones, fluoride in the water-bear-

ing soil and sediments substitutes into the original bone (Dwivedi et al., 1997; Wopenka and Pasteris, 2005). However, Cl^- does not substitute readily for OH^- groups due to its large ionic size, which obstructs the incorporation into the channel site. Cl-rich apatite is common in the geologic apatite samples with high temperatures formation (800-1,000 ℃) (Piccoli and Candela, 2002). Looking to the plots shown in Fig. 8, it is clear that blue bone deviates from the other three samples of the same group. The Cl^- content is higher and that correlates with the chlorapatite structure assigned to its XRD pattern. Blue color in apatite is commonly associated to Mn^{5+} at the P site (Reinen et al., 1986; Dardenne et al., 1999; Hughes et al., 2004). However, no bands corresponding to the presence of Mn have been observed in the blue bone spectrum and the EMPA analysis of this cation are below the limit detection. Robles and co-workers (2002), suggested Mn in small quantities as an element that can provide intensive blue coloration to minerals by incorporating into defective structures. The existence of Mn^{5+} in apatites is quite well established (Yubao et al., 1993; Mayer et al., 2003; Chadefaux et al., 2009), however, the presence in our samples could not be demonstrated directly with the non-destructive techniques.

The minor element composition makes a change to difference with the white sample (whiB). In this case, important substitutions of Ca by Na and Fe can be observed (Fig. 8d and 8f). From the XRD results one can infer a higher degree of crystallinity due to the diagenesis which generally influences entering of the elements into the crystal structure (Kalvoda et al., 2009). White color has been associated in the literature to an increase in the temperature (Lamsihar et al., 2015). Also, it is well known that as the temperature increases, the intensity and sharpening of the peaks increases.

Depositional Environments

Finally, it is important to note that local sedimentary factors influencing the mobilization of the components also control the introduction of some elements into the materials during fossilization. The difference between the green, white, and gray samples probably reflects different depositional environments in which the bones have been fossilized. According to Fesharaki (2016) there are different processes of formation of carbonate cements in the form of irregular patches in these sites. However, these carbonate cements do not occur in the areas with abundance of neoformed clay coatings. According to this author, it is possible that local pH variations were the cause of this differential cementation, which could be triggered by changes in groundwater height, a common process in areas with variations in temperature and precipitation in semi-arid environments (Bustillo and Alonso-Zarza, 2003, 2007; Carrasco et al., 2008). On the other hand, the micritic carbonates enclosing detrital grains and occasionally interbedded with smectitic clays, have a different origin. This origin seems to be related to both, the formation in a soil environment and the involvement of micro-organisms (bacteria). Different types of microorganisms have been observed in the studied samples (see an example of the surface of the green sample in the SEM images in Fig. 9). These microorganisms have been mainly associated with levels rich in calcretes and irregular micritic carbonates (Fesharaki, 2016). In this case, both, the formation and textures of these levels and the great variability of compositions observed in the smectites may be due to the biological action of these bacteria. All these processes would partly explain the local microenvironments favouring different activities of the existing chemical elements and, therefore, compositional, and possibly colour variations of the fossil samples.

Conclusions

The present research intended to apply different non-destructive techniques to characterize the mineralogical composition of the fossil bones from the Húmera paleontological site (Madrid, Spain) and the possible origin of the different colors shown in the samples. From our research, it is possible to not only identify the several mineralogical and textural characteristics in the coexisting samples, but also unravel the possible origin of the different colors. Namely, 6 colors have been identified and the Raman and XRD studies have permitted to classify the samples into three different types according to different characteristics.

Type I group of samples includes the gray, green, white and blue samples, which according to Raman and XRD analyses have been classified as fluorapatite in the first three cases, and chlorapatite in the case of the blue samples. Moreover, in both cases, fluorapatite and chlorapatite phases, the samples contain organic matter and adsorbed water. The presence of Mn^{5+} in apatite is associated with the existence of Mn^{5+} at the P site, however, the presence should be demonstrated with some other techniques. The red bone includes in the Type II samples, showing intermediate characteristics between samples from Type I and III. The broad Raman bands and the broad Bragg peaks shown for

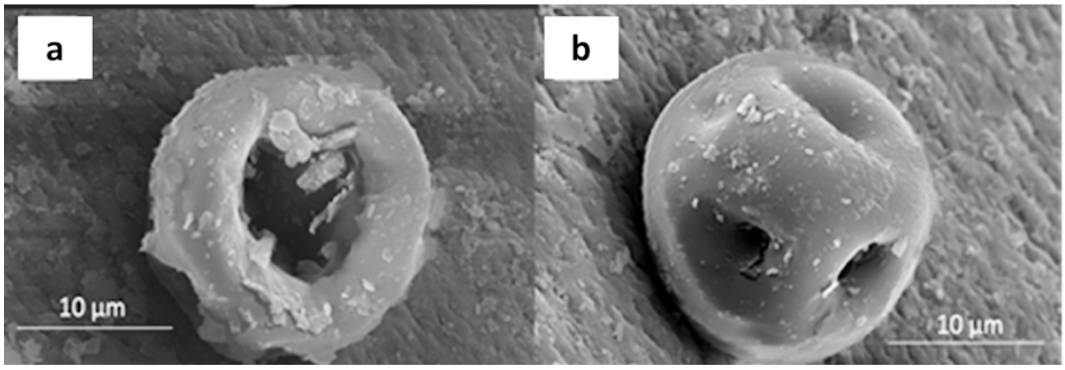

Figure 9. SEM images of the microorganisms observed on the surface of the green sample.

this sample emerge from both, the higher organic matter content found in the chemical composition, and the lattice disorder created by the B-type substitutions. These characteristics lead to classify this bone as bioapatite. Moreover, the red color could be also attributed to this high content in organic material. The yellow bone belonging to the Type III sample show a complete replacement of the bone by calcite. Moreover, it shows abundant porosity which has been attributed to the important decrease in the molar volume due to the replacement of the apatite bone by calcite.

Acknowledgements

This study was supported by the Ministry of Science, Innovation and Universities (CIENCIA) (Spain) under projects CGL2013-47988-C2-01-P and CGL2016-77138-C2-1-P. We thank to the directors of the excavations of the Húmera site, María Presumido and Juan Antonio Cárdaba (GEOSFERA), who obtained the corresponding prospecting and excavation permits commissioned and sponsored by the National Museum of Natural Sciences (CSIC), as well as to all the professors and students of the UCM who helped in these excavation and sediment samples preparation. The authors gratefully thank anonymous reviewers for the helpful corrections.

References

Antonakos, A., Liarokapis, E., and Leventouri, T., 2007, Micro-Raman and FTIR studies of synthetic and natural apatites. Biomaterials, v. 19, pp. 3043–3054.

Borrero, L.A., 2003, Taphonomy of the Tres Arroyos Rockshelter. Quaternary International, v. 109–110, pp. 87–93.

Brugmann, G., Kraus, J., Brachert, T.C., Stoll, B. Weis, U. Kullmer, O., Ssemmanda, I., and Mertz, D.F., 2012, Chemical composition of modern and fossil hippopotamid teeth and implications for paleoenvironmental reconstructions and enamel formation – Part 2: Alkaline earth elements as tracers of watershed hydrochemistry and provenance. Biogeosciences, v. 9, pp. 4803–4817.

Bustillo, M.A., and Alonso-Zarza, A.M., 2003, Transformaciones edaficas y diageneticas de los depositos aluviales distales del Mioceno de la cuenca de Madrid, area de Paracuellos de Jarama. Estudios Geológicos, v. 59, pp. 39–52.

Bustillo, M.A., and Alonso-Zarza, A.M., 2007, Overlapping of pedogenesis and meteoric diagenesis in distal alluvial and shallow lacustrine deposits in the Madrid Miocene Basin, Spain. Sedimentary Geology, v. 198, pp. 255–271.

Calvo, J.P., Alonso Zarza, A.M., and García del Cura, M.A., 1989, Models of Miocene marginal lacustrine sedimentation in response to varied depositional regimes and source areas in the Madrid Basin (Central Spain). Palaeogeography, Palaeoclimatology, Palaeoecology, v. 70, pp. 199–214.

Camacho, N.P., Rinnerthaler, S., Paschalis, E.P., Mendelsohn, R., Boskey, A.L., and Fratzl, P., 1999, Complementary information on bone ultrastructure from scanning small angle X-ray scattering and Fourier-transform infrared microspectroscopy. Bone, v. 25, pp. 287–293.

Cárdaba, J. A., Presumido, M., Fesharaki, O., Casado, A.I., Perales, R., and Muñiz Pérez, M., 2013, New data on the mammalian systematics and biostratigraphy of the middle Miocene from Húmera (Pozuelo de Alarcón). Spanish Journal of Paleontology, v. 28, pp. 29–42.

Carden, A., and Morris, M.D., 2000, Application of vibrational spectroscopy to the study of mineralized tissues (review). Journal of Biomedical Optics, v. 5, pp. 259–268.

Carrasco, A., Sacristan, S., Benitez-Lopez, G., Romero-Nieto, D., Fesharaki, O., and Lopez-Martinez, N., 2008, Aplicaciones paleoclimaticas y paleoambientales de los estudios mineralogicos al yacimiento de vertebrados miocenos de Somosaguas. In: Palaeontologica Nova (J. Esteve & G. Melendez, Eds.), Publicaciones del Seminario de Paleontologia de Zaragoza, v. 8, pp. 135–149.

Chadefaux, C., Vignaud, V., Chalmin, E., Robles-Camacho, J., Arroyo-Cabrales, J., Johnson, E., and Reiche, I., 2009, Color origin and heat evidence of paleontological bones: Case study of blue and gray vones from San Josecito Cave, Mexico. American Mineralogist, v. 94, pp. 27–33.

Clarke, J.B., and Barker, M.J., 1993, Diagenesis in Iguanodon bones from the Wealden Group, Isle of Wight, southern England. Kaupia Darmstdten Beitrage zur Naturgieschichte, v. 2, pp. 57–65.

Daculsi, G., Bouler, J.M., and LeGeros, R.Z., 1997, Adaptive crystal formation in normal and pathological calcifications in synthetic calcium phosphate and related biomaterials. International Review of Cytology - a Survey of Cell Biology, v. 172, pp. 129–191.

Dardenne, K., Vivien, D., and Huguenin, D., 1999, Color of Mn (V)-Substituted Apatites $A_{10}((B, Mn)O_4)_6F_2$, A=Ba, Sr, Ca; B=P, V. Journal of Solid State Chemistry, v. 146, pp. 464–472.

Dauphin, Y., 2023, A Brief History of Biomineralization Studies. Biomaterials Science and Engineering, v. 9, pp. 1774–1790.

Dwivedi, S.K., Dey, S., and Swarup, D., 1997, Hydrofluorosis in water buffalo (Bubalus bubalis) in India. The Science of the Total Environment, v. 207, pp.105–109.

Domingo, M.S., Martín-Peréa, D., Domingo, L., Cantero, E., Cantalapiedra, J.L., Yelo, B.A.G., Fesharaki, O., and Fernández, M.H., 2017, Taphonomy of mammalian fossil bones from the debris-flow deposits of Somosaguas-North (Middle Miocene, Madrid Basin, Spain). Palaeogeography, Palaeoclimatology, Palaeoecology, v. 465, pp. 103–121.

Doval, M., García Santiago, P., Domínguez Díaz, M.C., and Brell, J.M., 1985, Mineralogía de las arcillas de las facies evaporíticas de la cuenca del Tajo. Trabajos de Geología, v. 15, pp. 267–274.

Elliott, S., Bartley, T., Delorme, E., Derby, P., Hunt, R., Lorenzini, T., Parker, V., Rohde, M.F., and Stoney, K., 1994, Structural requirements for addition of O-linked carbohydrate to recombinant erythropoietin. Biochemistry, v. 33, pp. 11237–11245.

Elliott, J.C., 2002, Calcium phosphate biominerals. Reviews in mineralogy and geochemistry, v. 48, pp. 427-453.

Fesharaki, O., 2016, Análisis paleoambiental y paleoclimático de los yacimientos de Somosaguas y Húmera (Mioceno Medio, Madrid): sedimentología, petrología, mineralogía y aplicación a divulgación e innovación educativa. Universidad Complutense de Madrid, 366pp.

Fesharaki, O., Arribas, J., and Lopez-Martinez, N., 2015, Composition of clastic sediments in the Somosaguas area (middle Miocene, Madrid Basin): insights into provenance and palaeoclimate. Journal of Iberian Geology, v. 41, pp. 205–222.

Fesharaki, O., Coruña Llopis, F., and Salas-Herrera, J., 2021, Espectroscopía de infrarrojos de la fracción arcillosa de la sucesión sedimentaria del yacimiento paleontológico de Húmera (Cuenca de Madrid). Geogaceta, v. 69, pp. 79–82.

Figueiredo, M., Fernando, A., Martins, G., Freitas, J., Judas, F., and Figueiredo, H., 2010, Effect of the calcination temperature on the composition and microstructure of hydroxyapatite derived from human and animal bone. Ceramics International, v. 36, pp. 2383–2393.

Fleet, M.E., 2009, Infrared spectra of carbonate apatites: ν2-Region bands. Biomaterials, v. 30, pp. 1473–1481.

Freeman, J.J., Wopenka, B., Silva, M.J., and Pasteris, J.D., 2001, Raman spectroscopic detection of changes in bioapatite in mouse femora as a function of age and in vitro fluoride treatment. Calcified tissue international, v. 68, pp. 156–162.

Gadaleta, S.J., Paschalis, E.P., Betts, F., Mendelsohn, R., and Boskey,

A.L., 1996, Fourier transform infrared spectroscopy of the solution-mediated conversion of amorphous calcium phosphate to hydroxyapatite: new correlations between X-ray diffraction and infrared data. Calcified tissue international, v. 58, pp. 9–16.

Gross, K.A., and Berndt, C.C., 2002, Biomedical application of apatites. Reviews in mineralogy and geochemistry, v. 48, pp. 631–672.

Hedges, R. E., 2002, Bone diagenesis: an overview of processes. Archaeometry, v. 44, pp. 319–328.

Hedges, R.E.M., and Millard, A.R., 1995, Measurements and relationships of diagenetic alteration of bone from three archaeological sites. Journal of Archaeological Science, v. 22, pp. 201–209.

Hernando-Alonso, I., Fesharaki, O., Sánchez-Pastor, N., Casado, A.I., Astilleros, J.M., Lobato, A., Taravillo, M., and Fernández-Díaz, L., 2016, Caracterización química de fósiles del yacimiento de Húmera (Madrid) mediante técnicas no destructivas – Interpretación del origen del color. Macla, v. 21, pp. 56–58.

Hughes, J.M., and Pakovan, J., 2002, The Crystal Structure of Apatite, $Ca_2(PO_4)_3(F,OH,Cl)$. Reviews in Mineralogy and Geochemistry, v. 48, pp. 1–12.

Hughes, J. M., Ertl, A., Bernhardt, H-J., Rossman, G. R., and Rakovan, J., 2004, Mn-rich fluorapatite from Austria: Crystal structure, chemical analysis, and spectroscopic investigations. American Mineralogist, v. 89, pp. 629–632.

Jans, M.M.E., Nielsen-Marsh, C.M., Smith, C.I., Collins, M.J., and Kars, H., 2004, Characterisation of microbial attack on archaeological bone. Journal of Archaeological Science, v. 31, pp. 87–95.

Kalvoda, J., Novák, M., Bábek, O., Brzobohatý, R., Holá, M., Holoubek, I., Kanicky, V., and Škoda, R., 2009, Compositional changes in fish scale hydroxylapatite during early diagenesis; an example from an abandoned meander. Biogeochemistry, v. 94, pp. 197–215.

Kohn, B., Spiegel, C., Phillips, D., and Gleadow, A., 2008, Rubbing out apatite helium age-spread in fast-cooled rocks. In Proceedings from the 11th International Conference on Thermochronometry, Anchorage, Alaska, p. 144.

Laetsch, T., and Downs, R., 2006, Software for identification and refinement of cell parameters from powder diffraction data of minerals using the Rruff Project and American Mineralogist crystal structure databases. Abstracts from the 19th General Meeting of the International Mineralogical Association, Kobe, Japan.

Lamsihar Manalu, J., Soegijono, B., and Jusiana Indrani, D., 2015, Characterization of hydroxyapatite derived from bovine bone. Asian Journal of Applied Sciences, v. 3, pp. 758–765.

Landis, E., Celottia, G., Logroscinob, G., and Tampieria, A., 2003. Carbonated hydroxyapatite as bone substitute. Journal of the European Ceramic Society, v. 23, pp. 2931–2937.

Lebon, M., Reiche, I., Fröhlich, F., Bahain, J.J., and Falguères, C., 2008, Characterization of archaeological burnt bones: contribution of a new analytical protocol based on derivative FTIR spectroscopy and curve fitting of the ν_1 ν_3 PO_4 domain. Analytical and Bioanalytical Chemistry, v. 392, pp. 1479-1488.

Lebon, M., Reiche, I., Bahain, J.J., Chadefaux, C., Moigne, A.M., Fröhlich, F., Sémah, F., Schwarcz, H.P., and Falguéres, C., 2010, New parameters for the characterization of diagenetic alterations and heat-induced changes of fossil bone mineral using Fourier transform infrared spectrometry. Journal of Archaeological Science, v. 37, pp. 2265–2276.

LeGeros, R.Z., Trautz, O.R., Klein, E., and LeGeros, J.P., 1969, Two types of carbonate substitution in the apatite structure. Experientia, v. 25, pp. 5–7.

Mann, S., 2001, Biomineralization: principles and concepts in bioinorganic materials chemistry. Oxford University Press, pp. 198.

Mayer, I., Jacobsohn, O., Niazov, T., Werckman, J., Iliescu, M., Richard-Plouet, M., Burghaus, O., and Reinen, D., 2003, Manganese in precipitated hydroxyapatites. European Journal of Inorganic Chemistry, v. 7, pp. 1445–1451.

McConnell, D., and Gruner, J.W., 1940, The problem of the carbonate-apatites. III. Carbonate-apatite from Magnet Cove, Arkansas. American Mineralogist: Journal of Earth and Planetary Materials, v. 25, pp. 157–167.

McElderry, J.D.P., Zhu, P., Mroue, K.H., Xu, J., Pavan, B., Fang, M., Zhao, G., McNerny, E., Kohn, D.H., Franceschi, R.T., Banaszak Holl, M.M., Tecklenburg, M.M.J., Ramamoorthy, A., and Morris, M.D., 2013, Crystallinity and compositional changes in carbonated apatites: Evidence from ^{31}P solid-state NMR, Raman, and AFM analysis. Journal of solid state chemistry, v. 206, pp. 192–198.

Megias, A.G., Ordóñez, S., and Calvo, J.P., 1983, Nuevas aportaciones al conocimiento geológico de la Cuenca de Madrid. Revista de Materiales y Procesos Geológicos, v. 1, pp. 163–191.

Menéndez Gamella, A., Serrano, H., Presumido, M., Cárdaba, J.A., and Fesharaki, O., 2010, Húmera palaeontological sites (middle miocene Madrid basin): preliminary results in stratigraphy and palaeontology. Cidaris, v. 30, pp. 187–196.

Michel, V., Falguères, C., and Dolo, J.M., 1998, ESR signal behaviour study at g~ 2.002 of modern and fossil bones for heating palaeotemperature assessment. Radiation measurements, v. 29, pp. 95–103.

Michel, V., Bocherens, H., Théry-Parisot, I., Valoch, K., and Valensi, P., 2006, Colouring and preservation state of faunal remains from the Neanderthal levels of Kulna Cave, Czech Republic. Geoarcheology: An International Journal, v. 21, pp. 479–501.

Millard, A., and Hedges, R., 1996, A diffusion-adsorption model of uranium uptake by archaeological bone. Geochimica et Cosmochimica Acta, v. 60, pp. 2139–2152.

Montel, G., Bonel, G., Heughebaert, J.C., Trombe, J.C., and Rey, C., 1981, New concepts in the composition, crystallization and growth of the mineral component of calcified tissues. Journal of Crystal Growth, v. 53, pp. 74–99.

Montes, M., Beamud, B., Garcés, M., and Calvo, J.P., 2006, Magnetoestratigrafía de las Unidades Inferior e Intermedia del Mioceno de la Cuenca de Madrid. Revista de la Sociedad Geológica de España, v. 19, pp. 281–298.

Nicholson, R.A., 1993, A Morphological Investigation of Burnt Animal Bone and an Evaluation of its Utility in Archaeology. Journal of Archaeological Science, v. 20. pp. 411–428.

Nielsen-Marsh, C.M., and Hedges, R.E., 2000, Patterns of Diagenesis in Bone I: The Effects of Site Environments. Journal of Archaeological Science, v. 27, pp. 1139–1150.

Nielsen-Marsh, C.M., Smith, C.I., Jans, M.M.E., Nord, A., Kars, H., and Collins, M.J., 2007, Bone diagenesis in the European Holocene II: taphonomic and environmental considerations. Journal of Archaeological Science, v. 34, pp. 1523–1531.

Pan, Y., and Fleet, M.E., 2002, Compositions of the apatite-group minerals: substitution mechanisms and controlling factors. Reviews in mineralogy and geochemistry, v. 48, pp. 13–49.

Pasteris, J.D., Freeman, J.J., Goffredi, S.K., and Buck, K.R., 2001, Raman spectroscopic and laser scanning confocal microscopic analysis of sulfur in living sulfur-precipitating marine bacteria. Chemical Geology, v. 180, pp. 3–18.

Pasteris, J.D., Wopenka, B., Freeman, J.J., Rogers, K.D., Valsami-Jones, E., Van der Houwen, J.A.M., and Silva, M.J., 2004, Lack of OH in nanocrystalline apatite as a function of degree of atomic order: implications for bone and biomaterials. Biomaterials, v. 25, pp. 229–238.

Penel, G., Leroy, G., Rey, C., and Bres, E., 1998, MicroRaman spectral study of the PO_4 and CO_3 vibrational modes in synthetic and biological apatites. Calcified tissue international, v. 63, pp. 475–481.

Penel, G., Delfosse, C., Descamps, M., and Leroy, G., 2005, Composition of bone and apatitic biomaterials as revealed by intravital Raman microspectroscopy. Bone, v. 36, pp. 893–901.

Person, A., Bocherens, H., Saliége, J-F., Paris, F., Zeitoun, V., and Gérard, M., 1995, Early diagenetic evolution of bone phosphate: an x-ray diffractometry analysis. Journal of Archaeological Science, v. 22, pp. 211–221.

Piccoli, M., and Candela, P.A, 2002, Apatite in Igneous Systems. Reviews in Mineralogy and Geochemistry, v. 48, pp. 255–292.

Pieczka, A., Golebiowska, B., Jelén, P., Sitarz, M., and Szuszkiewicz, A., 2020, Raman spectroscopic studies of O–H stretching vibration in Mn-rich apatites: A structural approach. American Mineralogist, v. 105, pp. 1385–1391.

Piga, G., Santos-Cubedo, A., Brunetti, A., Piccinini, M., Malgosa, A., Napolitano, E., and Enzo, S., 2011, A multi-technique approach by XRD, XRF, FT-IR to characterize the diagenesis of dinosaur bones from Spain Palaeogeography, Palaeoclimatology, Palaeoecology, v. 310, pp. 92–107.

Reiche, I., Vignaud, C., and Menu, M., 2002, The crystallinity of ancient bone and dentine: new insights by transmission electron microscopy. Archaeometry, v. 44, pp. 447–459.

Reinen, D., Lachwa, H., and Allmann, R., 1986, EPR- und ligandenfeldspektroskopische Untersuchungen an Mn^{V}-haltigen Apatiten sowie die Struktur von $Ba_5(MnO_4)_3Cl$. Zeitschrift für anorganische und allgemeine Chemie , v. 542, pp. 71–88.

Rey, C., Collins, B., Goehl, T., Dickson, I.R., and Glimcher, M.J., 1989, The carbonate environment in bone mineral - A resolution-enhanced Fourier transform infrared spectroscopy study. Calcified Tissue International, v. 45, pp. 157–164.

Rey, C., Shimizu, M., Collins, B., and Glimcher, M.J., 1990, Resolution-enhanced Fourier transform infrared spectroscopy study of the environment of phosphate ion in the early deposits of a solid phase of calcium phosphate in bone and enamel and their evolution with age: Investigations in the n_4PO_4 domain. Calcified Tissue International, v. 46, pp. 384–394.

Rhodes, S.E., Walker, M.J., López-Jiménez, A., López-Martínez, M., Haber-Uriarte, M., Fernández-Jalvo, Y. and Chazan, M., 2016, Fire in the Early Palaeolithic: Evidence from burnt small mammal bones at Cueva Negra del Estrecho del Río Quípar, Murcia, Spain. Journal of Archaeological Science, v. 9, pp. 427–436.

Robles, J., Arroyo-Cabrales, J., Johnson, E., Allen, B.L., and Izquierdo, G., 2002, Blue bone analyses as a contribution to the study of bone taphonomy in San Josecito Cave, Nuevo Leon, Mexico. Journal of Cave and Karst Studies, v. 64, pp. 145–149.

Sabel, N., Klinberg, G., Nietsche, S., Robertson, A., Odelius, H., and Noren, J., 2009, Analysis of some elements in primary enamel during postnatal mineralization, Swedish Dental Journal, v. 33, pp. 85–95.

Shahack-Gross, R., Bar-Yosef, O., and Weiner, S., 1997, Black-coloured bones in Hayonim cave, Israel: Differentiating between burning and oxide staining. Journal of Archaeological Science, v. 24, pp. 439–446.

Shipman, P., Foster, G., and Schoeninger, M., 1984, Burnt bones and teeth: an experimental study of color, morphology, crystal structure and shrinkage. Journal of archaeological science, v. 11, pp. 307–325.

Sponheimer, M., and Lee-Thorp, J.A., 1999, Alteration of enamel carbonate environments during fossilization. Journal of Archaeological Science, v. 26, pp. 143–150.

Stathopoulou, E.T., Psycharis, V., Chryssikos, G.D., Gionis, V., and Theodorou, G., 2008, Bone diagenesis: New data from infrared spectroscopy and X-ray diffraction. Palaeogeography, Palaeoclimatology, Palaeoecology, v. 266, pp. 168–174.

Tadic, D., and Epple, M., 2004, A thorough physicochemical characterisation of 14 calcium phosphate-based bone substitution materials in comparison to natural bone. Biomaterials, v. 25, pp. 987–994.

Tarnowski, C.P., Ignelzi Jr, M.A., and Morris, M.D., 2002, Mineralization of developing mouse calvaria as revealed by Raman microspectroscopy. Journal of bone and Mineral Research, v. 17, pp. 1118–1126.

Thomas, D.B., Fordyce, R.E., Frew, R.D., and Gordon, K.C., 2007, A rapid, non-destructive method of detecting diagenetic alteration in fossil bone using Raman spectroscopy. Journal of Raman Spectroscopy, v. 38, pp. 1533–1537.

Timlin, J.A., Carden, A., and Morris, M.D., 1999, Chemical microstructure of cortical bone probed by Raman transects. Applied Spectroscopy, v. 53, pp. 1429–1435.

Torres, T., Maldonado, A., Querol, R., and Zamora, I., 1995, Evolución en el subsuelo de los sistemas de abanicos aluviales del Mioceno de la cuenca de Madrid (España). Geogaceta, v. 18, pp. 56–58.

Trueman, C.N.G., Behrensmeyerb, A.K., Turossc, N., and Weinerd, E., 2004, Mineralogical and compositional changes in bones exposed on soil surfaces in Amboseli National Park, Kenya: diagenetic mechanisms and the role of sediment pore fluids. Journal of Archaeological Science, v. 31, pp. 721–739.

Weiner, S., and Wagner, H.D., 1998, The material bone: structure-mechanical function relations. Annual Review of Materials Research, v. 28, pp. 271–298.

Weiner, S., and Price, P.A., 1986, Disaggregation of bone into crystals. Calcified tissue international, v. 39, pp. 365–375.

Weiner, S., Traub, W., and Wagner, H.D., 1999, Lamellar bone: structure–function relations. Journal of structural biology, v. 126, pp. 241–255.

Wojdyr, M., 2010, Fityk: a general-purpose peak fitting program. Journal of applied crystallography, v. 43, pp. 1126–1128.

Wopenka, B., and Pasteris, J.D., 2005. A mineralogical perspective on the apatite in bone. Materials Science and Engineering., v. 25, pp. 131–143.

Xue, W., Zhaim, S., and Xu, S., 2015, Photoluminescence properties of γ-$Ca_3(PO_4)_2$:Sm^{3+} prepared under high-pressure and high-temperature conditions. Optical Materials, v. 45, pp. 219–233.

Yubao, L., Klein, C.P.A.T., Xingdong, Z., and de Groot, K., 1993, Relationship between the colour change of hydroxyapatite and the trace element manganese. Biomaterials, v. 14, pp. 969–972.

Nuria Sánchez-Pastor is currently working as a Senior Lecturer in the Department of Mineralogy and Petrology at the Faculty of Geological Sciences, Complutense University of Madrid, Spain. She has extensive experience in using surface and structural characterization techniques, such as X-ray diffraction, Raman spectroscopy, and Atomic Force Microscopy. She specializes in the study of crystallization processes at low temperatures and under mild hydrothermal conditions. Her main scientific interest focuses on solvent-mediated mineral transformations and mineral replacement reactions, with an emphasis on understanding diagenetic processes and pollutant uptake by mineral surfaces (decontamination of heavy metals through sorption processes).

Omid Fesharaki is a researcher and lecturer at the Faculty of Education at Complutense University of Madrid, Spain. He holds a PhD in Geology from the same university. His research interests focus on the multidisciplinary analysis of paleoenvironments and the study of educational curricula for primary and secondary education, aiming to propose motivating activities and methodological teaching improvements. He is a member of the organizing committee of the Madrid Geology Olympics and participates in various Teaching Innovation and Service-Learning projects across several universities in Madrid. These projects involve numerous geology teaching and dissemination activities, especially targeting people with functional diversity.

Isabel Hernando-Alonso graduated in Geology from the University of Salamanca (2012-2016). She subsequently completed a Master's in Geological Processes and Resources at the Complutense University of Madrid in 2017, and a Master's in Teaching Biology and Geology in 2019. She has previously worked as an exploration geologist and laboratory technician at CENIEH, participating in various projects. Currently, she is pursuing her PhD at CENIEH, funded by MINCIU and FEDER, focusing on the geological context of the Atapuerca sites in the Duero Basin. Her research employs Electron Spin Resonance (ESR) to characterize and date fluvial and karstic sediments.